Homogenised Optoelectronic Properties in Perovskites: Achieving High-Efficiency Solar Cells with Common Chloride Additives

Junke Wang[1,†], Shuaifeng Hu[1,†], Xinyu Gu[2,†], Minh Anh Truong[3,†], Yi Yang[4,†], Cheng Liu[4], Gunnar Kusch[5], Zhongcheng Yuan[1], Manuel Kober-Czerny[1], Zuhong Zhang[6], Zhenhuang Su[7], Kyohei Nakano[8], Akash Dasgupta[1], Xianfu Zhang[4], Xinyi Shen[1], Nobutaka Shioya[3], Noriko Kurose[9], Daichi Shirakura[10], Zaiwei Wang[11], Wei Zhou[12], Meng Li[6], Takeshi Hasegawa[3], Xingyu Gao[7], Keisuke Tajima[8], Rachel A. Oliver[5], Yixin Zhao[2], Zhijun Ning[12,*], Atsushi Wakamiya[3,*], Henry J. Snaith[1,*] and Hao Chen[2*]

[1]Clarendon Laboratory, Department of Physics, Parks Road, Oxford OX1 3PU, United Kingdom

[2]Centre of Future Photovoltaics Research, Global Institute of Future Technology, Shanghai Jiao Tong University, Shanghai 200240, China

[3]Institute for Chemical Research, Kyoto University, Gokasho, Uji, Kyoto 611-0011, Japan

[4]Institute of Chemical Sciences and Engineering, École Polytechnique Fédérale de Lausanne, EPFL VALAIS, Sion 1951, Switzerland

[5]Department of Materials Science and Metallurgy, University of Cambridge, Cambridge CB3 0FS, United Kingdom

[6]Key Lab for Special Functional Materials of Ministry of Education, School of Nanoscience and Materials Engineering, Henan University, Kaifeng 475004, China

[7]Shanghai Synchrotron Radiation Facility, Shanghai Advanced Research Institute, Chinese Academy of Sciences, 239 Zhangheng Road, Shanghai 201204, China

[8]RIKEN Centre for Emergent Matter Science (CEMS), Wako, Saitama 351-0198, Japan

[9]RIKEN Center for Advanced Photonics (RAP), 2-1, Wako-shi, Saitama 351-0198, Japan

[10]Surface Science Laboratories, Toray Research Centre, Inc., 3-3-7, Sonoyama, Otsu, Shiga 520-8567, Japan

[11]Institute of Technology for Carbon Neutrality, Shenzhen Institute of Advanced Technology, Chinese Academy of Sciences, Shenzhen 518055, China

[12]School of Physical Science and Technology, ShanghaiTech University, Shanghai 201210, China

Email: ningzhj@shanghaitech.edu.cn; wakamiya@scl.kyoto-u.ac.jp; henry.snaith@physics.ox.ac.uk; hao.chen1@sjtu.edu.cn

[†]These authors contributed equally

Methods

Materials. Unless otherwise stated, all the materials were used as received without further purification. Cesium iodide (CsI, >99%), methylammonium iodide (MAI, >99.0%, low water content), formamidinium iodide (FAI, >98.0%, low water content), lead(II) iodide (PbI_2, 99.99%, trace metals basis), methylammonium chloride (MACl, >98.0%), lead(II) chloride ($PbCl_2$, >99.0%, for Perovskite precursor), [2-(9H-carbazol-9-yl)ethyl]phosphonic acid (2PACz, >98.0%), and [4-(3,6-dimethyl-9H-carbazol-9-yl)butyl]phosphonic acid (Me-4PACz, >99.0%) were purchased from Tokyo Chemical Industry Co., Ltd. (TCI). Phenethylammonium iodide (PEAI) and ethane-1,2-diammonium iodide ($EDAI_2$) were purchased from Greatcell Solar Materials. Fullerene C_{60} (sublimed, 99.99%) was purchased from ATR Company. NiO_x nanoparticles were synthesized following our previously reported method[1]. Dehydrated isopropanol, ethanol, anisole, *N,N*-dimethylformamide (DMF), and dimethyl sulfoxide (DMSO) were purchased from Sigma-Aldrich without further treatment.

Solar cell fabrication. For p-i-n structured solar cells, NiO_x (5 mg mL^{-1} in H_2O:IPA solution [3:1, v/v) was spin-coated on cleaned FTO substrates in the air at 3000 rpm for 30 s (3 s acceleration to 3000 rpm) without any post-treatment. Then, a mixture of 2PACz and Me-4PACz (2:1, w:w) in ethanol (0.5 mg mL^{-1}) was spin-coated inside an N_2-filled glovebox at 3000 rpm for 30 s (3 s acceleration to 3000 rpm) and the substrates were annealed at 120 °C for about 10 min. The perovskite film was prepared in a N_2-filled glove box (H_2O, O_2 < 0.1 ppm). The $Cs_{0.05}FA_{0.9}MA_{0.05}PbI_3$ perovskite precursor solution was prepared by mixing CsI (19.5 mg, 0.075 mmol), MAI (12.0 mg, 0.075 mmol), FAI (232.2 mg, 1.35 mmol), and PbI_2 (691.5 mg, 1.50 mmol) in a solvent mixture of 0.20 mL DMSO and 0.80 mL DMF to reach a concentration of 1.5 M for the control sample. For the MACl-added sample, MACl (13 mg, 13 mol% vs PbI_2) was added to the control solution. For the $PbCl_2$-added sample, $PbCl_2$ (13 mg, 3 mol% vs PbI_2) was added to the control solution. For the MACl + $PbCl_2$-added sample, MACl (13 mg, 13 mol% vs

PbI_2) and $PbCl_2$ (13 mg, 3 mol% vs PbI_2) were added to the control solution. The precursor solutions were stirred at 50 °C for about 1 h and filtered through a 0.20 µm PTFE filter before use. To spin coat the films, 200 µL of the precursor solution was applied to the substrate. A two-step spin coating program was used. The first step was 1000 rpm for 10 s with an acceleration of 1000 rpm s^{-1}, and the second was 5000 rpm for 30 s with a ramp-up of 500 rpm s^{-1}. As an antisolvent, 150 µL anisole at room temperature was dripped onto the surface of the spinning substrate 5 seconds before the end of the spinning program. Then, the film was immediately annealed at 120 °C for 10 min. For the surface passivation, a mixture of PEAI and $EDAI_2$ (1:0.5, w/w) was dissolved in IPA at a concentration of 1.0 mg mL^{-1} and spin-coated on the perovskite film at 4000 r.p.m. for 30 s with an acceleration of 2000 r.p.m per second, as we reported before[2-6]. The substrates were then transferred to a thermal evaporator to deposit 20 nm of C_{60} at a rate of 0.2 Å s^{-1}. 20 nm of SnO_x was then deposited using temporal atomic-layer-deposition using Picosun. For the top contact, 120 nm of Ag was deposited in a thermal evaporator. The cell has an active area of 0.05 or 1.0 cm^2.

PV performance characterisation. The *J–V* characteristics were measured in N_2 at room temperature using a Keithley 2400 source meter. A Sciencetech A1 Light Line Class AAA solar simulator was used to simulate AM 1.5G irradiation (100 mW cm^{-2}) with an Xe arc lamp intensity. The light intensity was calibrated by a Sciencetech SCI-REF-Q Si reference cell. The scanning step was 20 mV and the scanning rate was 70 mV s^{-1}. The device active area was determined by a shadow mask of 0.05 or 1 cm^2 placed in front of the solar cell pixel. The EQE spectra were measured in the ambient by QE-R, Enlitech.

Stability testing. A homebuilt tracking station was used to perform solar cell stability measurements. A UV-free white LED with calibrated 1-sun intensity was used as the light source, similar to our previous work[7]. For the MPPT test, encapsulated solar cells were operated under continuous 1 sun illumination and mounted on a metal plate at 65 ℃ using a heating element, monitored by a thermal couple. The device chamber was left open in a room with 50 ± 10% relative humidity. For the thermal stability analysis, encapsulated devices were stored in the dark at 85 ℃ in N_2. Device encapsulation was performed by covering a capping glass slide on top with an ultraviolet-adhesive (Lumtec LT-U001) as the sealant.

Ex-situ GIWAXS measurements. GIWAXS measurements were performed using a Rigaku (Tokyo, Japan) SmartLab X-ray diffractometer equipped with a hybrid pixel array two-dimensional detector "HyPix-3000"[8]. Cu Kα radiation (λ = 0.15418 nm) was generated from a sealed-tube X-ray source operated at 40 kV and 50 mA. The angle of incidence was fixed at 0.200°, and the exposure time was 1000 s. The detector was placed 65.0 mm from the centre of the goniometer. In this optical configuration, no diffracted X-rays are detected in the region below q~2.0 nm^{-1}. The obtained images were converted to reciprocal space maps using the SmartLab Studio II software. Perovskite films were deposited on the top of 2PACz + Me-4PACz with glass/ITO as substrates to mimic the growth conditions in full devices. The sample-to-detector distance was 65 mm and the incidence angle was set to 0.4°.

ToF-SIMS measurements. ToF-SIMS measurements were carried out using an M6 (IONTOF GmbH). The depth profiles (**Fig. 2a**) were acquired in high mass resolution mode. A 60 keV Bi_3^{2+} primary ion beam with target current of 0.02 pA was used for data acquisition and mass resolution (M/ΔM) was 11300 at $^{35}Cl^-$ in the control sample. For sample etching, a 10 keV Ar_{1200}^+ gas cluster ion beam with target current of 14 nA was used as a sputtering ion beam. The raster area of the primary ion beam was 200 µm × 200 µm. ToF-SIMS 3D tomography (**Fig. 2b–c**) was acquired in high lateral resolution mode. A 60 keV Bi_3^{2+} primary ion beam with target current of 0.01 pA was used for data acquisition and mass resolution (M/ΔM) was 330 at $^{35}Cl^-$ in the control sample. For sample etching, a 10 keV Ar_{1200}^+ gas cluster ion beam with target current of 10 nA was used as a sputtering ion beam. The raster area of the primary ion beam was 30 µm × 30 µm.

To quantify the atomic concentration of chloride ions in ToF-SIMS analysis, we calculate the relative sensitivity factor of chloride (RSF_{Cl}) using the chloride atomic concentration obtained from X-ray photoelectron (XPS) measurements (see **Supplementary Fig. 7**) and the averaged normalised chloride intensity from the ToF-SIMS measurements. The analysis is performed on $PbCl_2$ and MACl + $PbCl_2$ samples, where distinct Cl 2p core level peaks are observed. Given that the typical analysis depth of XPS is approximately 10 nm, we utilise the averaged normalised chloride intensity from ToF-SIMS over the 0–10 nm depth range. The RSF_{Cl} is calculated using the following equation:

$$RSF_{Cl} = C_{Cl} \times (I_I / \gamma_I) / (I_{Cl} / \gamma_{Cl}) = C_{Cl} / (I_{Cl,norm.} / 0.758)$$

Where C_{Cl} is the Cl atomic concentration determined from XPS (**Supplementary Table 2**), I_I is the intensity of I from ToF-SIMS, γ_I is the isotope ratio of I ($\gamma_I = 1$), I_{Cl} is the intensity of Cl from ToF-SIMS, γ_{Cl} is the isotope ratio of Cl ($\gamma_{Cl} = 0.758$), and $I_{Cl,\ norm}$ is the averaged normalised Cl intensity from the ToF-SIMS measurements over the 0–10 nm depth range (**Supplementary Table 3**). Therefore, the residual Cl content is calculated using the following equation, where $RSF_{Cl,\ average}$ represents the averaged RSF value (**Supplementary Table 4**).

$$C_{Cl} = RSF_{Cl,average} \times (I_{Cl,norm.} / 0.758)$$

UPS measurements. UPS was performed with a photoelectron spectroscopy system (PHI5000 Versa Probe II, ULVACPHI Inc.) with He I excitation (21.22 eV). A −5.0 V bias was applied to the samples. The chamber base pressure was approximately 1×10^{-6} Pa. Samples were transferred from the glove box to the UPS chamber without exposure to air.

CL emission analysis. CL hyperspectral maps were measured by Attolight Allalin 4027 Chronos in a continuous wave mode at room temperature and under high vacuum. All the perovskite samples were prepared on glass/ITO/HTL half-stacks to ensure similar film quality compared to actual devices. The SEM and CL images were acquired at ~3 kV acceleration voltage and ~63 pA beam current. The pixel resolution was 128 × 128 in a 5 μm field of view. Energy bandpass-filtered images were generated by integrating the CL intensities over specific energy ranges. The spectra of individual pixels and line scans and the spatially averaged spectra were analysed by an open-source software package[9].

In-situ GIWAXS. The synchrotron-based in situ grazing-incidence wide-angle X-ray scattering (GIWAXS) experiments were conducted at the BL14B1 beamline of the Shanghai Synchrotron Radiation Facility (SSRF). The X-ray beam had a wavelength of 1.24 Å and an energy of 10 keV. A MarCCD 225 area detector was employed to collect two-dimensional (2D) GIWAXS patterns, with a sample-to-detector distance of 330 mm. This incidence angle was set at 0.4 degree, and the measurements were recorded at the start of the spin coating. The stage of the spin coater was accelerated to 5000 rpm in about 10 s and kept at 5000 rpm for 40 seconds, during which 200 μL of chlorobenzene (CB) was added at the 30-second mark, in a dry air glovebox. Following spin-coating, an annealing under 150 and 120 °C was applied for the control and the rest of the samples, respectively, for up to 300 seconds.

In-situ PL. The *in-situ* PL spectra were collected with a home-built PL setup placed in a nitrogen glovebox. All the precursor films were place on the stage of the setup right after spin-coating process and then excited with a LED light souces (light intensity around 15 mW cm^{-2}). A QE PRO spectrometer (Ocean Optics) coupled with a optical fiber was use to collected emisson continuously.

Luminescence imaging. The QFLS imaging analysis was performed on full PSCs using a homebuilt setup reported previously[10]. A 450 nm LED (Thorlabs, M450LP1) was used to illuminate the solar cell from the glass side, with the photon flux calibrated to be ~1-sun intensity for the perovskite absorbers under study (powered by Multicomp PRO MP710086 ben power supply). The solar cells were electrically biased by a Keithley 2400 source meter, through a multiplexing circuit and sample holder designed in-house. The PL images were acquired by an Andor Zyla 4.2 sCMOS sensor, cooled at 0 ˚C, and equipped with a Kowa LM50XC lens (50 mm, with up to an F2.0 aperture). To image the entire device area, the aperture was set to F5.6 to increase the depth of field.

Time-resolved photoluminescence. The TRPL response of perovskite thin films with different Cl additives was determined using time-correlated single photon counting (TCSPC) with a FluoTime300 (Picoquant). The samples were excited at a repetition rate of 50 kHz using a 405 nm pulsed diode laser (LDH-P-C-405, Picoquant). A single photon counting electronics (TimeHarp260 nano, Picoquant) was coupled to the PMT detector (dead time < 95 ps) that collected the emitted PL. The TCSPC method requires that all detected photons are single photons. To ensure this, the pile-up rate, which is the ratio of the rate of emission to the rate of excitation, must be minimal. We therefore maintained a pile-up rate of less than 5% for all measurements carried out during this study. To extract physical parameters from the TRPL decays, we excited each sample at two fluences (1.3×10^{9} cm^{-2} and 1.3×10^{10} cm^{-2}), as well as from the substrate (bottom) and perovskite (top) side.

Extracting parameters from TRPL measurements using Bayesian Inference. We co-assess a set of four measurements (two intensities from the top side and two from the bottom side) with a recently reported method. In brief, we simulate TRPL decays using eight parameters and a comprehensive physical model. Values for the parameters are picked by a no-U-Turn Markov-chain Monte-Carlo (MCMC) algorithm. We then use Bayesian inference to estimate the probability that a simulated TRPL curves agrees with the data. As a result, we

obtain a probability histograms for each parameter, as depicted in **Supplementary Fig. 21–24**, which indicate the number of times each value of a given parameter was picked. Using this method, we can differentiate between the recombination happening at the perovskite-air surface (S_{top}) and in the perovskite bulk. We could not confidently determine any value for the vertical charge carrier mobility, which can happen, if the charge carrier density is too low[11,12]. In that case, the impact of the vertical diffusion on the overall TRPL response is too small to be used for the inference. We hence used a different methodology for this parameter afterwards.

Vertical mobility from the spectral shift. To estimate the vertical mobility, we follow an approach by Cho. et.al.[13]. Pulsed photoexcitation results in a high electron and hole density in the vicinity of the illuminated surface. PL is generated via band-to-band recombination of electrons and holes. As the charge carriers diffuse deeper into the film the emitted light may be re-absorbed by the perovskite material. Since this is more likely to happen for high energy photons, the PL spectra undergo an effective red shift. To estimate the shift of the PL peak, we use our TCSPC setup and measure the TRPL decay of the blue (750 nm) and red (850 nm) side individually. We illuminate the samples from the perovskite side with the same laser as used for the other measurements and a fluence of 1.3×10^{10} cm^{-2}. We then estimate the spectral shape via

$$r_{PL}(t) = \frac{PL(850\,nm, t)}{PL(750\,nm, t)} - 1 \qquad (1)$$

The resulting ratio of the PL is shown in **Supplementary Fig. 26** as a function of time. Similar to our own recent work[14], we can numerically solve the vertical diffusion equation to accurately determine the charge carrier density as a function of z-coordinate and time ($n(t,z)$). Here, we use the relation $D\mathrm{PL} = 0.5 \bullet D\mathrm{n}$. We can then use

$$PL_{rel.}(\lambda, t) = \int_0^d n(t, z)^2 \cdot e^{-\alpha_\lambda z}\, dz. \qquad (2)$$

to fit μ_{vert} from $r_{PL}(t)$, where α_λ is the absorption coefficient as obtained from UV-Vis absorption of ellipsometry. The result is shown in **Supplementary Fig. 26** as a solid line.

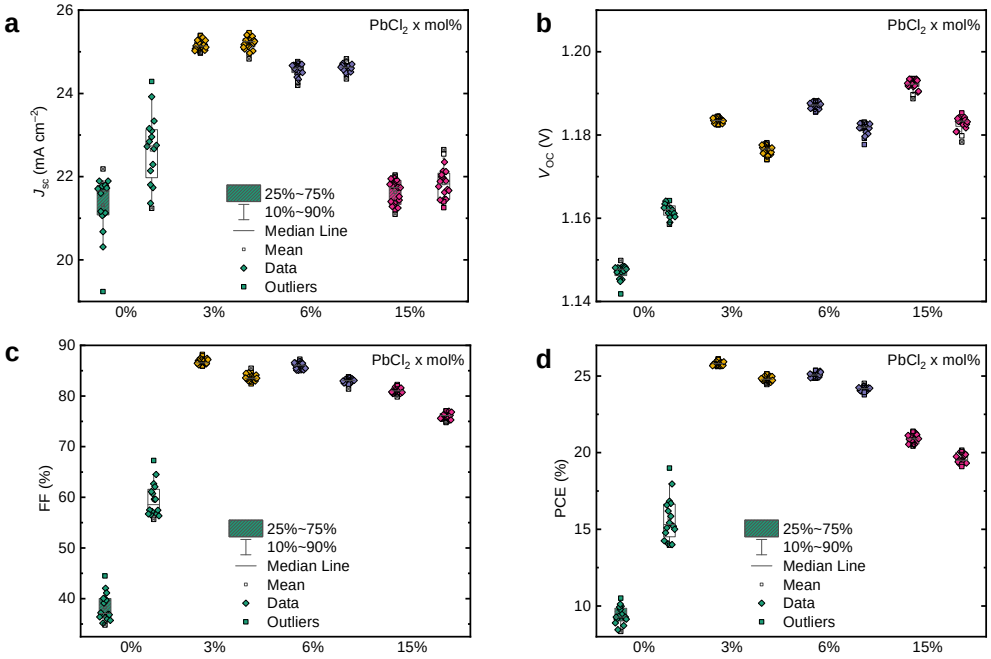

Supplementary Figure 1. Photovoltaic performance of the control (0 mol %), 3 mol%, 6 mol%, and 15 mol% of $PbCl_2$ added PSCs (0.05 cm²). For each variation, at least 16 devices were tested. In the boxplots, the mean (open square), median (centre line), 25th and 75th percentiles (box limits), minimum (–) and maximum (+), outliers (△), and 10th and 90th percentiles (whiskers) are shown. For each condition, the left column displays results under reverse scans, and the right column shows results under forward scans. Both the J_{SC} and FF increase substantially from 21.3 ± 0.7 mA cm^{-2} and 0.38 ± 0.03 for the control device (without any additives) to 25.2 ± 0.2 mA cm^{-2} and 0.87 ± 0.01 with the addition of 3 mol% $PbCl_2$ (reverse scans). This increases the average PCE from 9.3 ± 0.6% (reverse scans) for the control device to 25.8 ± 0.2% (reverse scans) for the 3 mol% $PbCl_2$ devices. However, adding more $PbCl_2$ reduces the cell performance, despite a slight increase in the V_{OC} up to 1.19 V at 15 mol% $PbCl_2$.

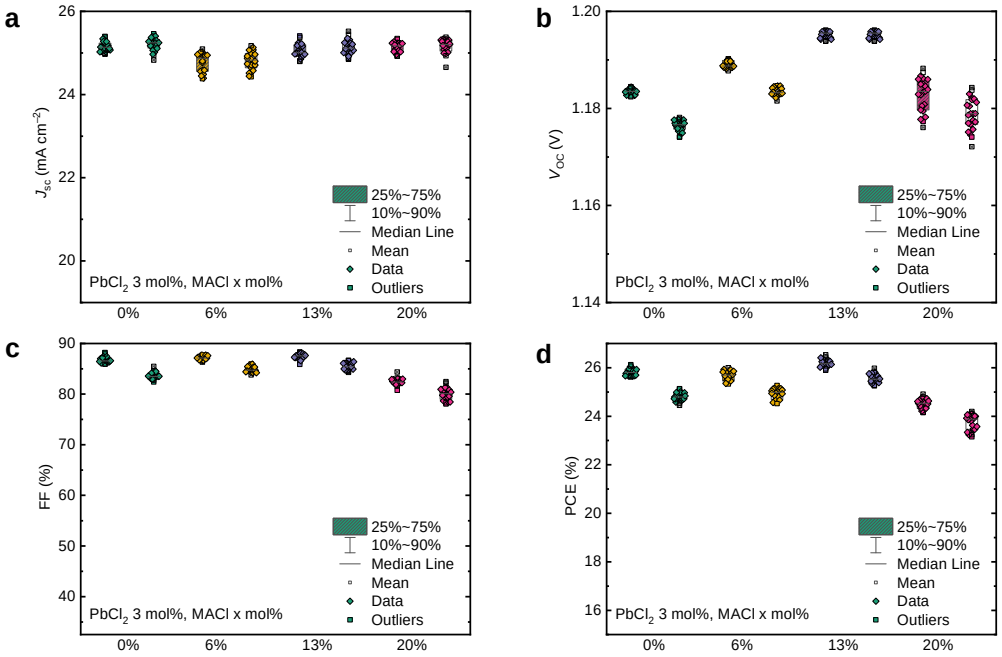

Supplementary Figure 2. Photovoltaic performance of the 3 mol% $PbCl_2$, with 0 mol%, 6 mol%, 13 mol%, and 20 mol% of MACl added PSCs (0.05 cm^2). For each variation at least 18 devices were tested. In the boxplots, the mean (open square), median (centre line), 25th and 75th percentiles (box limits), minimum (–) and maximum (+), outliers (△), and 10th and 90th percentiles (whiskers) are shown. For each condition, the left column displays results under reverse scans, and the right column shows results under forward scans. We find a further increase in the averaged V_{OC} from 1.18 V for the 3 mol% $PbCl_2$ devices to 1.20 V for the 3 mol% $PbCl_2$ + 13 mol% MACl devices, leading to the highest average PCE of 26.2 ± 0.2% (reverse scans). We note that increasing MACl content beyond this point reduces both the V_{OC} and FF and thereby the PCE. Based on these findings, we select 3 mol% $PbCl_2$ and 13 mol% MACl as our target concentrations for this study.

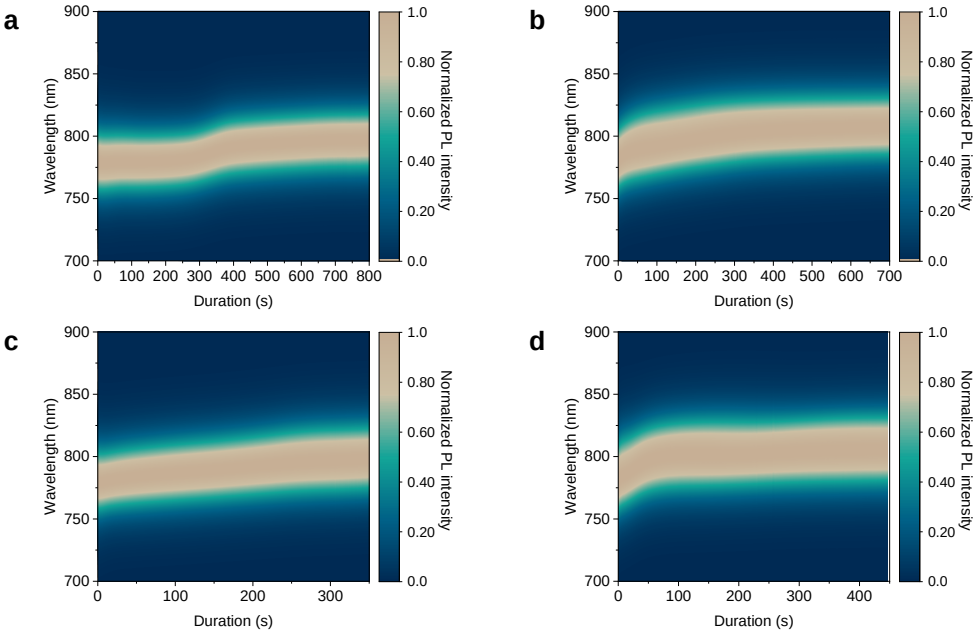

Supplementary Figure 3. Crystallisation dynamics. In-situ PL spectra of **a**, control, **b**, MACl, **c**, $PbCl_2$, and **d**, MACl + $PbCl_2$ perovskite precursor films after spin-coating.

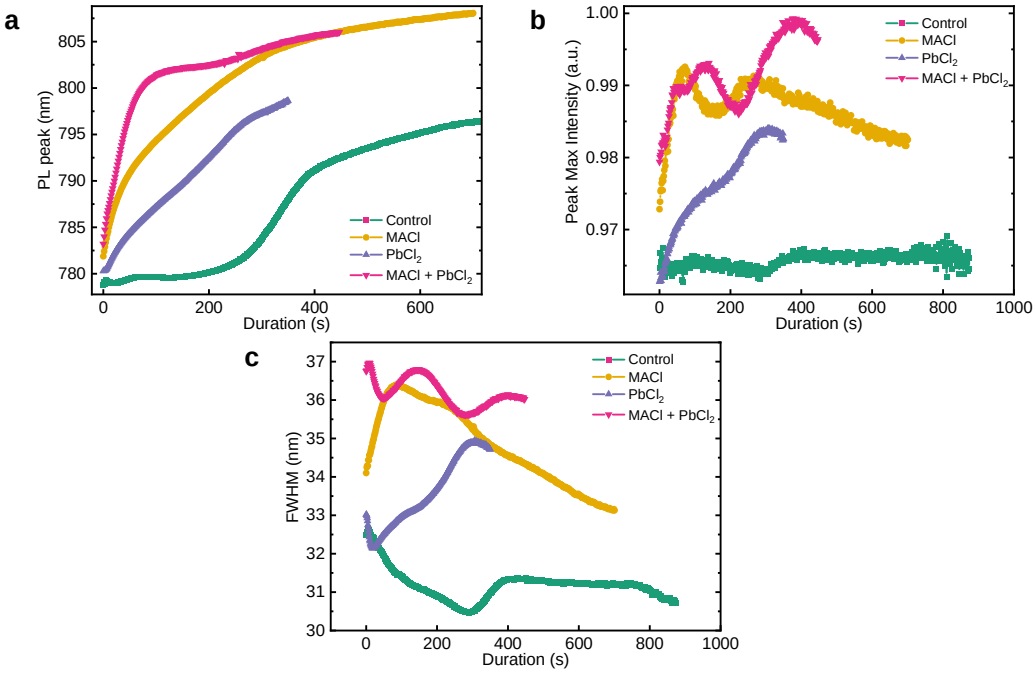

Supplementary Figure 4. Crystallisation dynamics. Extracted PL peak position (**a**), peak intensity (**b**), and full-width at half-maximum (FWHM) (**c**) from in-situ PL data (**Supplementary Fig. 3**).

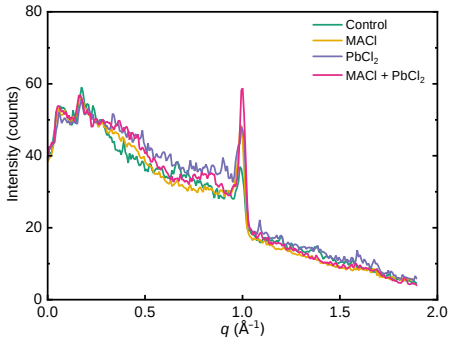

Supplementary Figure 5. Film crystallinity. Line profiles of post-annealed perovskite films derived from radially integrated 2D GIWAXS patterns (**Fig. 1b**).

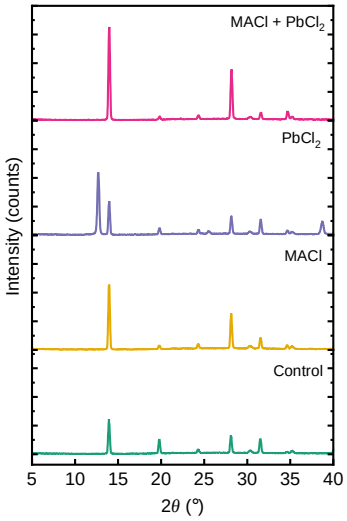

Supplementary Figure 6. Film crystallinity. 1D XRD patterns of the control, MACl, $PbCl_2$, and MACl + $PbCl_2$ perovskite samples.

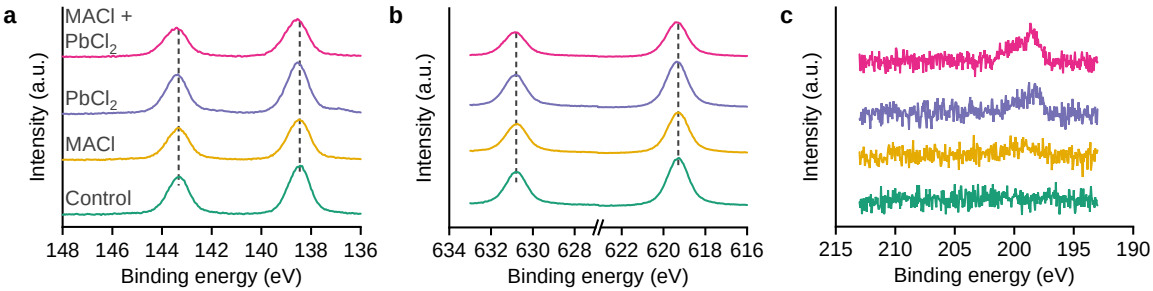

Supplementary Figure 7. Elemental analysis of perovskite films. XPS spectra of **a**, Pb 4*f*, **b**, I 3*d*, and **c**, Cl 2*p* core levels. The amount of Cl is increased gradually for the control, MACl, $PbCl_2$, and MACl + $PbCl_2$ samples. The corresponding atomic concentrations for all samples are displayed in **Supplementary Table 2**.

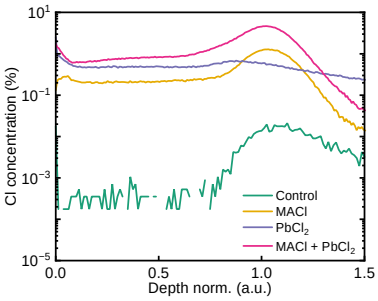

Supplementary Figure 8. Elemental analysis of perovskite films. ToF-SIMS depth profile of quantified chloride anion concentrations using calibrated relative sensitivity factor for chloride. The calculation of RSF factors in ToF-SIMS is provided in the **Methods** section and the corresponding normalised intensity and relative sensitivity factor of chloride are provided in **Supplementary Table 3–4.**

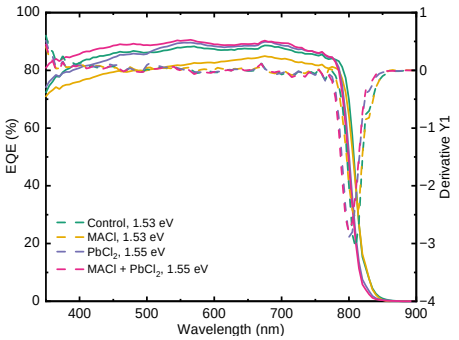

Supplementary Figure 9. EQE spectra. The external quantum efficiency (EQE) spectra and their first derivative as a function of photon energy of control, MACl, $PbCl_2$, and MACl + $PbCl_2$ PSCs.

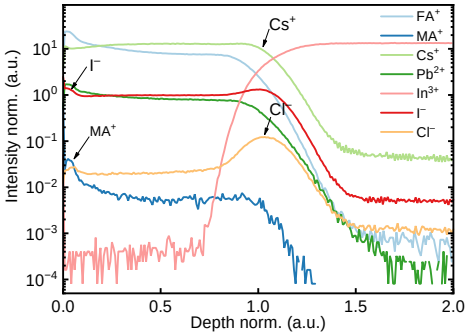

Supplementary Figure 10. Elemental analysis of perovskite films. ToF-SIMS depth profiles of MACl perovskite film.

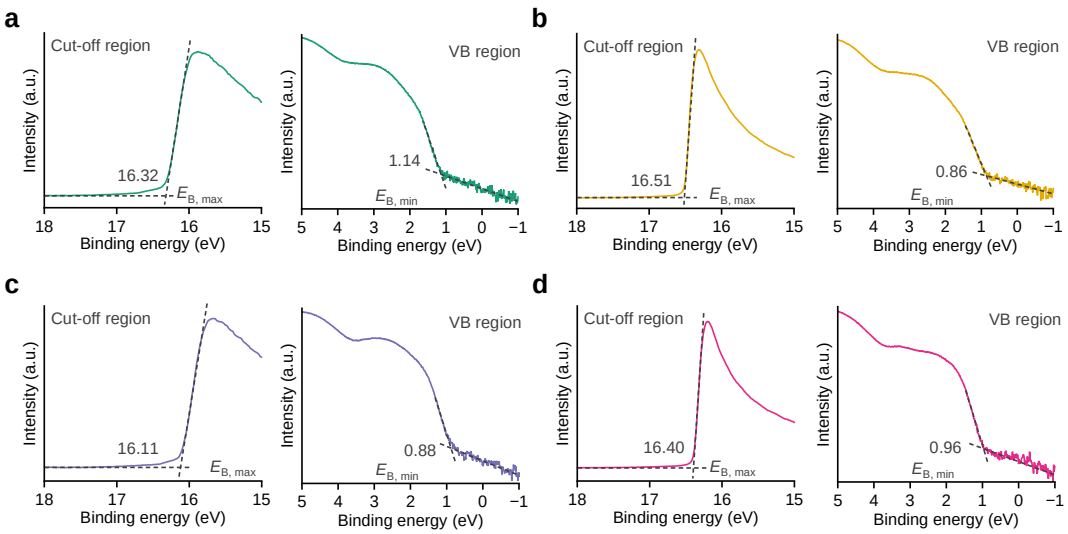

Supplementary Figure 11. Electronic structure of perovskite films. Secondary electron cut-off and valence band (VB) regions of the UPS spectra for the perovskite films ($Cs_{0.05}FA_{0.90}MA_{0.05}PbI_3$) fabricated **a,** without additive, and with the addition of, **b**, MACl, **c**, $PbCl_2$, and **d**, MACl + $PbCl_2$. The work function (WF) of the perovskite films is 21.22 eV – $E_{B,\ max}$, with $E_{B,\ max}$ determined from the secondary electron cut-off region. The VBM is –(21.22 eV – ($E_{B,\ max}$ – $E_{B,\ min}$)), with the $E_{B,\ min}$ determined from the VB region.

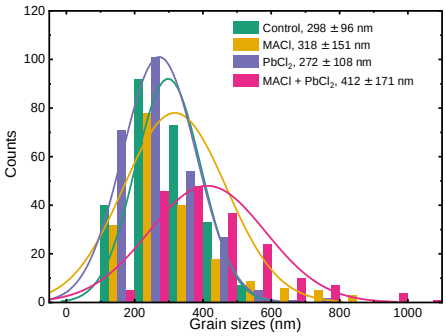

Supplementary Figure 12. Morphology of perovskite films. The grain size distribution of control, MACl, $PbCl_2$, and MACl + $PbCl_2$ perovskite films.

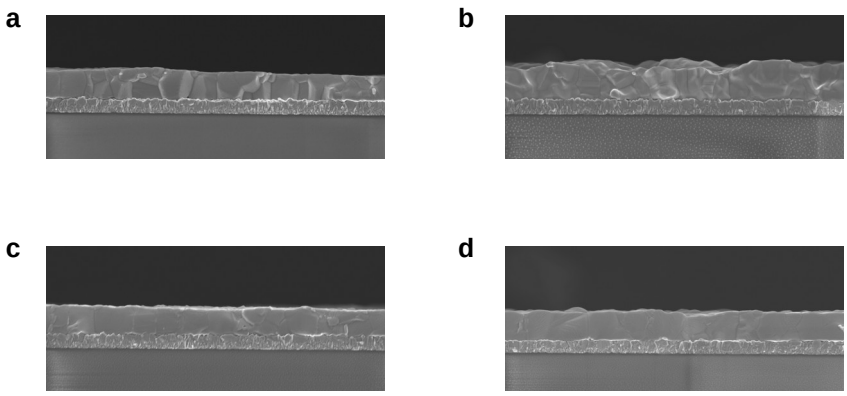

Supplementary Figure 13. Morphology of perovskite films. Cross-sectional SEM images of control, MACl, $PbCl_2$, and MACl + $PbCl_2$ perovskite films deposited on glass/ITO substrates. Scale bars are 1 μm.

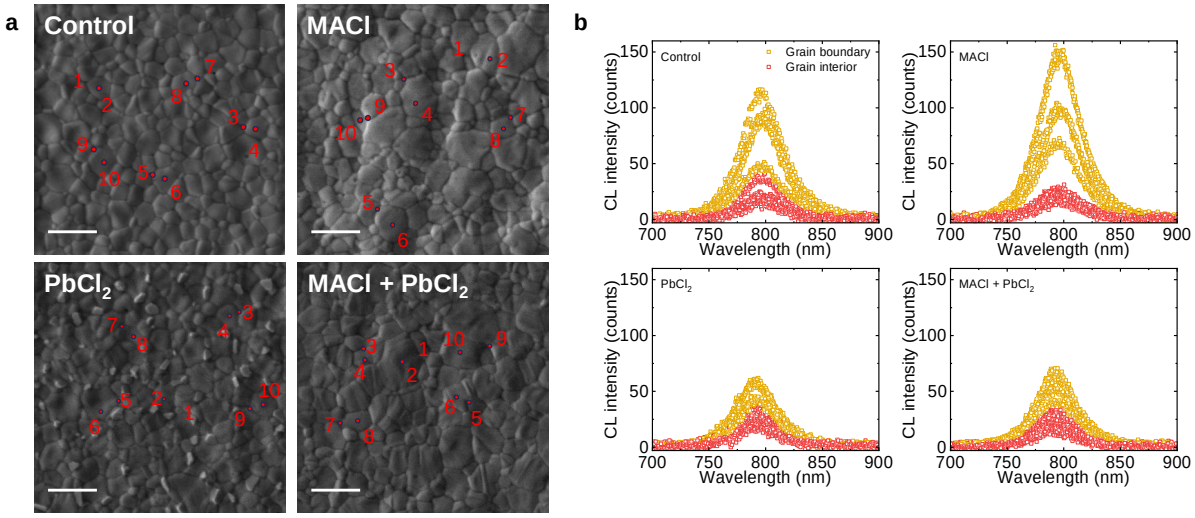

Supplementary Figure 14. Nanoscopic emission properties of perovskite films. a,**b**, The top-view SEM images (**a**) and the corresponding CL spectra (**b**) of control, MACl, $PbCl_2$, and MACl + $PbCl_2$ perovskite films. Scale bars are 1 μm. The CL spectra from the grain boundary regions (yellow) are drawn from pixels numbered as 1, 3, 5, 7, and 9. The spectra from the grain interiors (red) are drawn from pixels numbered as 2, 4, 6, 8, and 10.

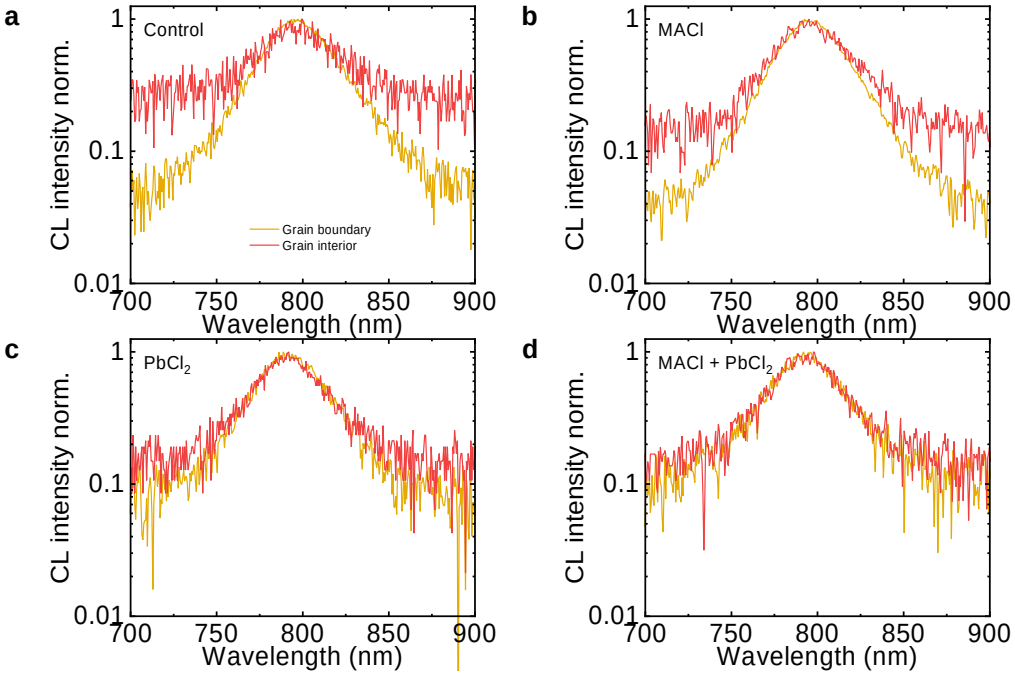

Supplementary Figure 15. Nanoscopic emission of perovskite films. Normalised CL point spectra of control (**a**), MACl (**b**), $PbCl_2$ (**c**), and MACl + $PbCl_2$ (**d**) perovskite films. The spectra from the grain boundary regions (yellow) are drawn from pixels numbered as 3, 1, 1, and 1, respectively, from **Supplementary Fig. 14**. The spectra from the grain interiors (red) are drawn from pixels numbered as 4, 2, 2, and 2, respectively, from **Supplementary Fig. 14**.

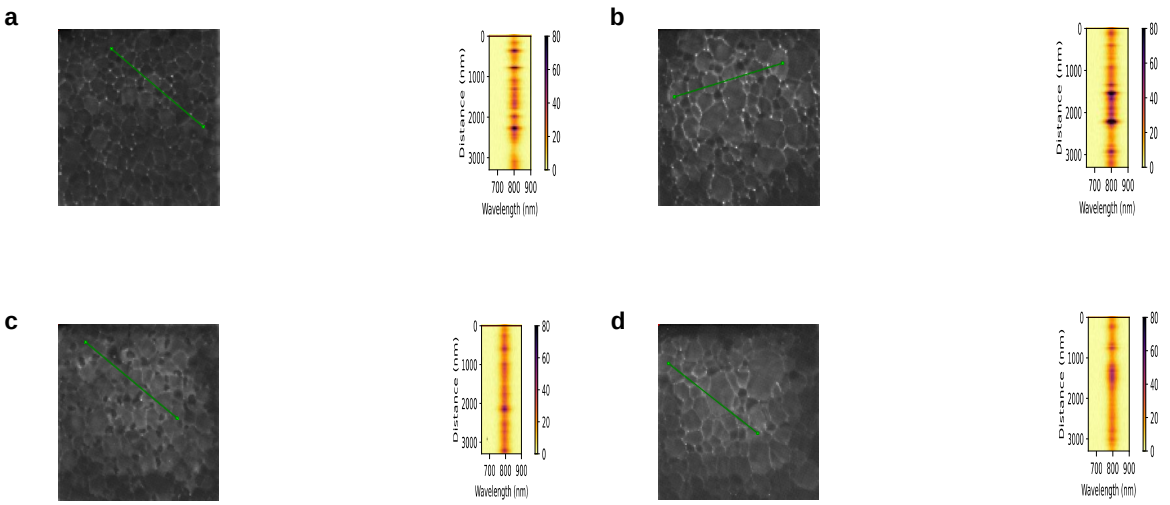

Supplementary Figure 16. Nanoscopic emission of perovskite films. CL line spectra of control, MACl, $PbCl_2$, and MACl + $PbCl_2$ perovskite films. Scale bars are 1 µm.

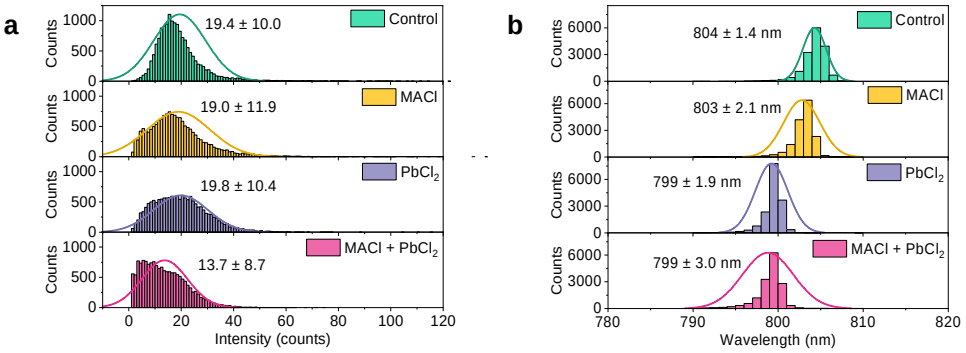

Supplementary Figure 17. Nanoscopic emission of perovskite films. a,**b**, The histogram of CL intensity (**a**) and the maximum emission wavelength (**b**) of control, MACl, $PbCl_2$, and MACl + $PbCl_2$ perovskite films.

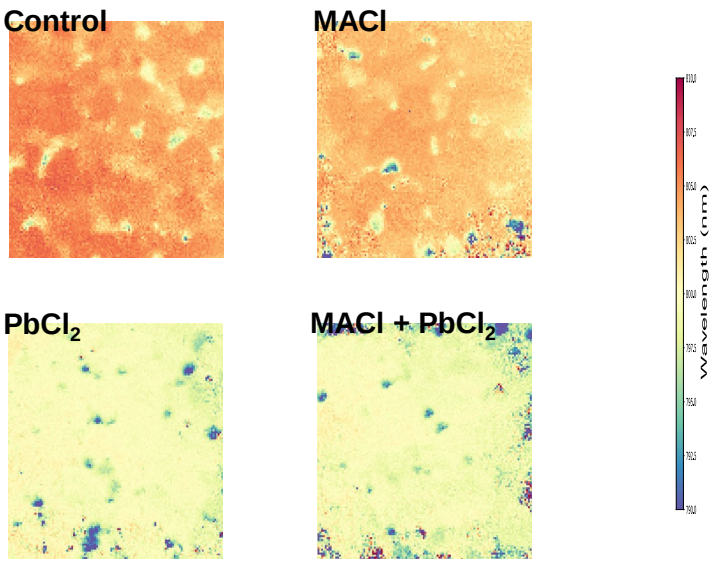

Supplementary Figure 18. Nanoscopic emission of perovskite films. CL hyperspectral images of control, MACl, $PbCl_2$, and MACl + $PbCl_2$ perovskite films in the wavelength region of 790−810 nm. Scale bars are 1 μm.

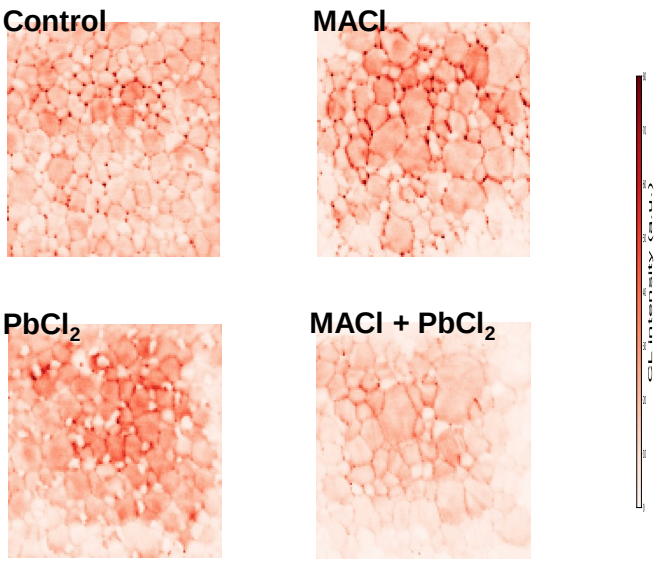

Supplementary Figure 19. Nanoscopic emission of perovskite films. CL maps of control, MACl, $PbCl_2$, and MACl + $PbCl_2$ perovskite films in the wavelength region of 790−810 nm. Scale bars are 1 μm.

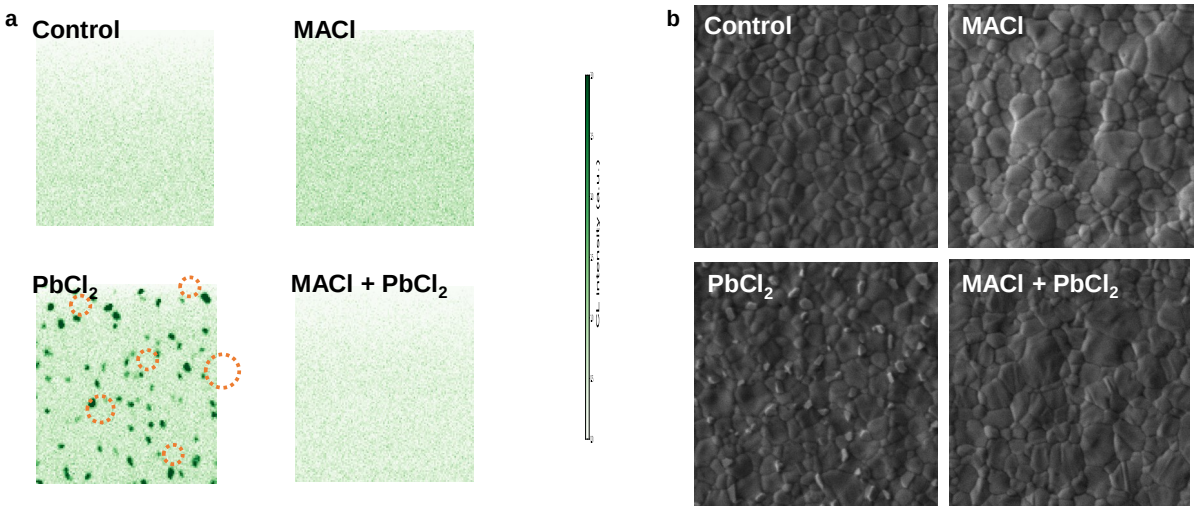

Supplementary Figure 20. Nanoscopic emission of perovskite films. a, CL maps of control, MACl, $PbCl_2$, and MACl + $PbCl_2$ perovskite films in the wavelength region of 510−550 nm. **b**, The corresponding SE images. Orange circles are drawn to highlight needle shaped features that are attributed to PbI_2. Scale bars are 1 µm.

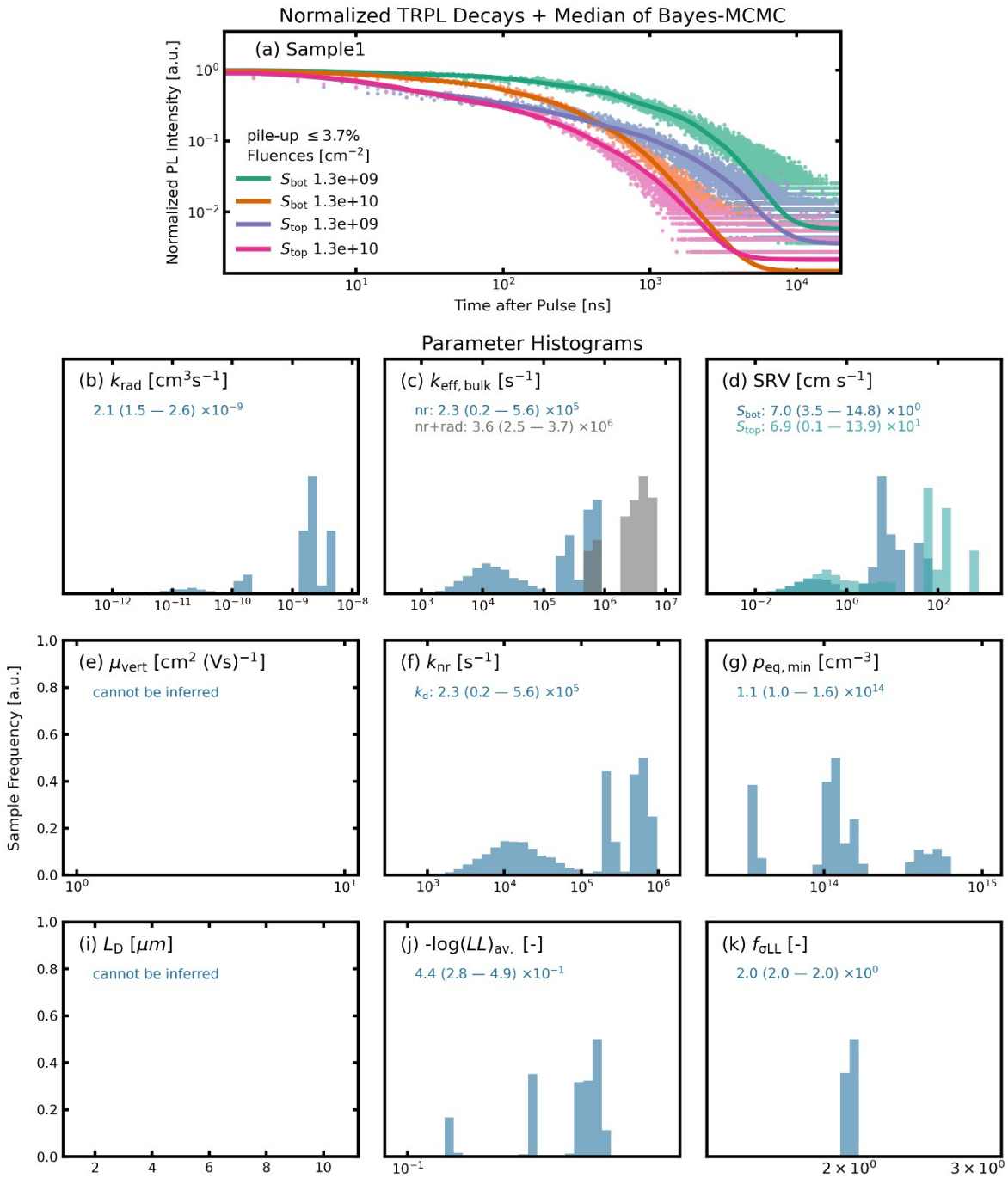

Supplementary Figure 21. Carrier dynamics of the control sample. a, TRPL decays measured from both the top (perovskite-air interface) and substrate (glass/ITO/HTL) sides. **b–k**, The normalised probability distributions for all parameters extract from the Bayes-MCMC, including the radiative recombination rate (k_{rad}), effective non-radiative bulk recombination rate ($k_{\text{eff, nr, bulk}}$), surface recombination rate (SRV), vertical mobility (μ_{vert}), non-radiative recombination rate via a deep bulk defect (k_{d}), equilibrium hole density under pulsed excitation

(p_{eq}), diffusion length (L_D), average log-likelihood for the dataset (–log(LL)$_{av}$), and $f_{\sigma LL}$.

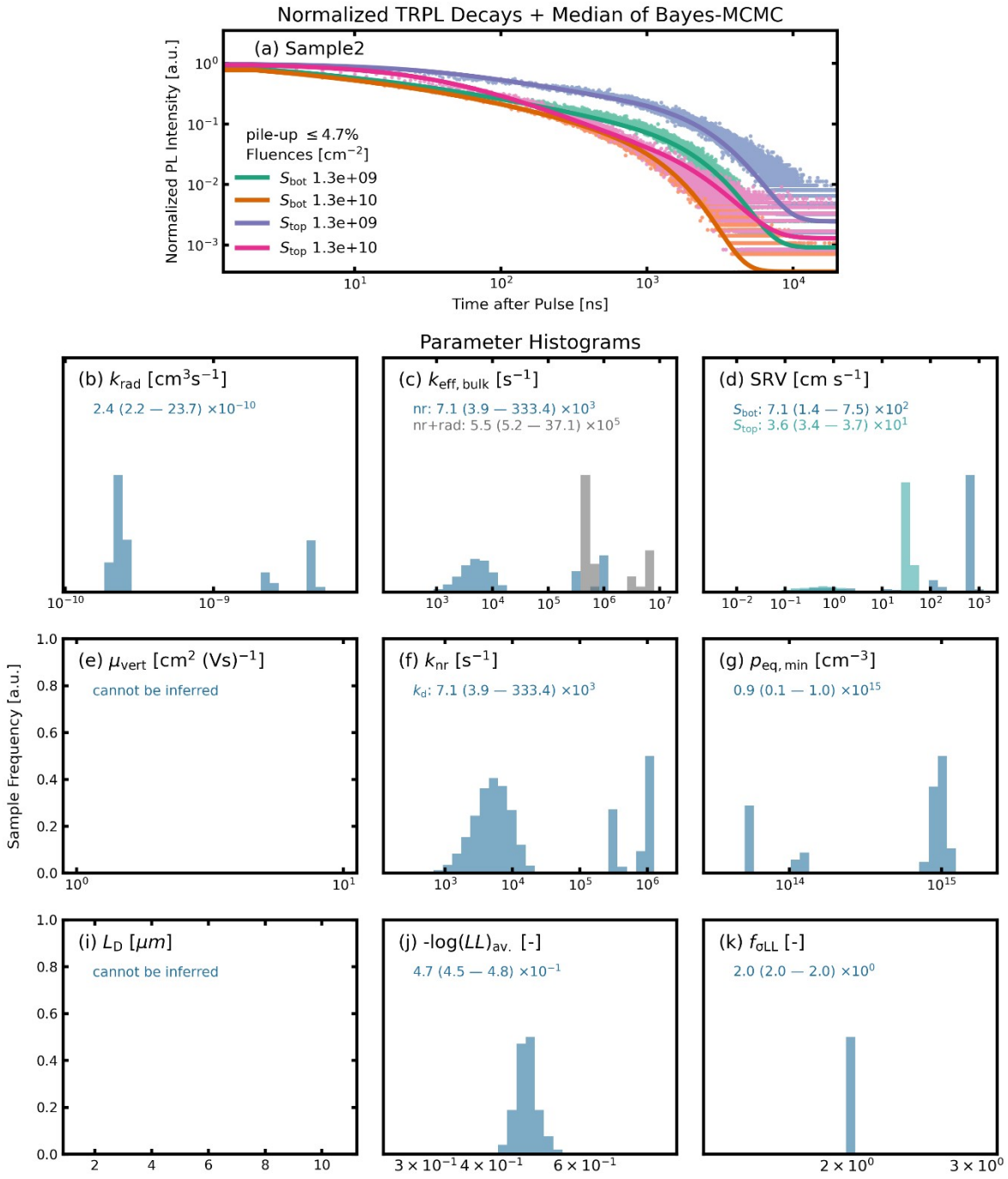

Supplementary Figure 22. Carrier dynamics of the MACl sample. a, TRPL decays measured from both the top (perovskite-air interface) and substrate (glass/ITO/HTL) sides. **b–k**, The normalised probability distributions for all parameters extract from the Bayes-MCMC, including the radiative recombination rate (k_{rad}), effective non-radiative bulk recombination rate ($k_{\mathrm{eff,\ nr,\ bulk}}$), surface recombination rate (SRV), vertical mobility (μ_{vert}), non-radiative recombination rate via a deep bulk defect (k_{d}), equilibrium hole density under pulsed excitation (p_{eq}), diffusion length (L_{D}), average log-likelihood for the dataset ($-\log(LL)_{\mathrm{av}}$), and $f_{\sigma LL}$.

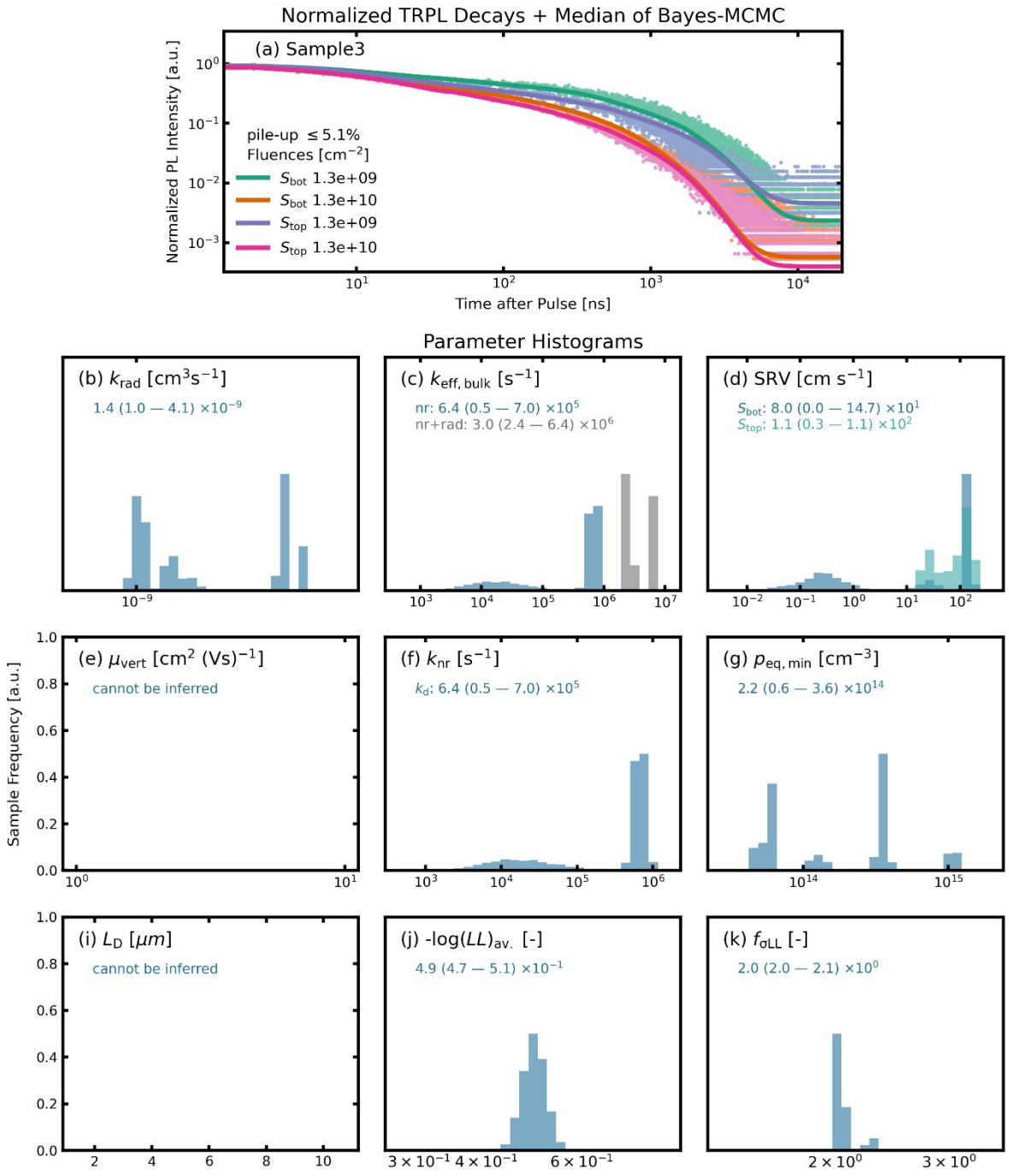
Normalized TRPL Decays + Median of Bayes-MCMC
(a) Sample3
Normalized PL Intensity [a.u.]
pile-up ≤ 5.1%
Fluences [cm^{-2}]
S_{bot} 1.3e+09
S_{bot} 1.3e+10
S_{top} 1.3e+09
S_{top} 1.3e+10
Time after Pulse [ns]
Parameter Histograms
(b) k_{rad} [cm^{3}s^{-1}]
1.4 (1.0 — 4.1) ×10^{-9}
(c) $k_{eff, bulk}$ [s^{-1}]
nr: 6.4 (0.5 — 7.0) ×10^5
nr+rad: 3.0 (2.4 — 6.4) ×10^6
(d) SRV [cm s^{-1}]
S_{bot}: 8.0 (0.0 — 14.7) ×10^1
S_{top}: 1.1 (0.3 — 1.1) ×10^2
Sample Frequency [a.u.]
(e) μ_{vert} [cm^2 (Vs)$^{-1}$]
cannot be inferred
(f) k_{nr} [s^{-1}]
k_d: 6.4 (0.5 — 7.0) ×10^5
(g) $p_{eq, min}$ [cm^{-3}]
2.2 (0.6 — 3.6) ×10^{14}
(i) L_D [μm]
cannot be inferred
(j) -log(LL)$_{av.}$ [-]
4.9 (4.7 — 5.1) ×10^{-1}
(k) $f_{\sigma LL}$ [-]
2.0 (2.0 — 2.1) ×10^0

Supplementary Figure 23. Carrier dynamics of the $PbCl_2$ sample. a, TRPL decays measured from both the top (perovskite-air interface) and substrate (glass/ITO/HTL) sides. **b–k**, The normalised probability distributions for all parameters extract from the Bayes-MCMC, including the radiative recombination rate (k_{rad}), effective non-radiative bulk recombination rate ($k_{\mathrm{eff,\ nr,\ bulk}}$), surface recombination rate (SRV), vertical mobility (μ_{vert}), non-radiative recombination rate via a deep bulk defect (k_{d}), equilibrium hole density under pulsed excitation (p_{eq}), diffusion length (L_{D}), average log-likelihood for the dataset ($-\log(LL)_{\mathrm{av}}$), and $f_{\sigma LL}$.

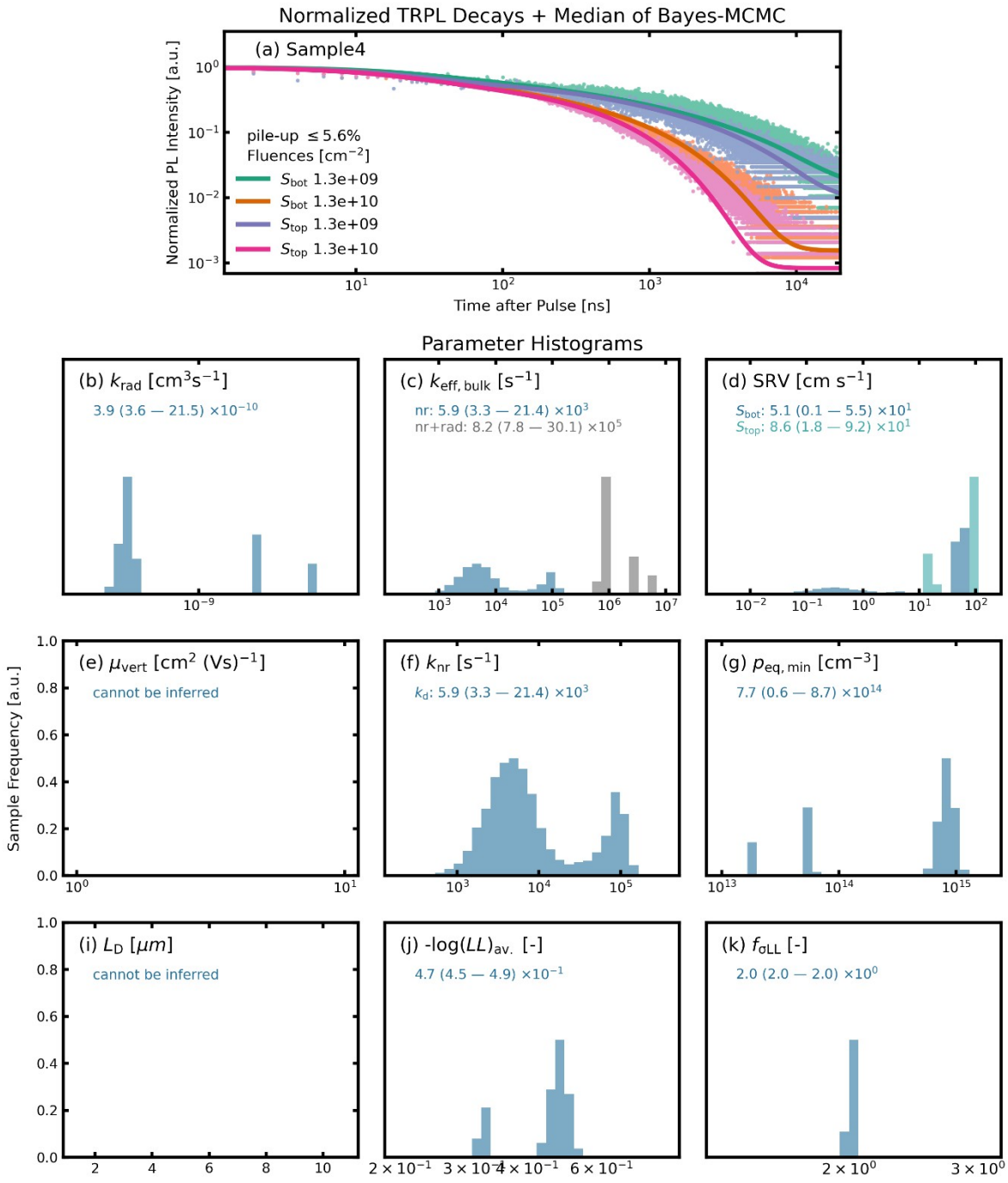
Normalized TRPL Decays + Median of Bayes-MCMC
(a) Sample4
pile-up ≤ 5.6%
Fluences [cm^{-2}]
S_{bot} 1.3e+09
S_{bot} 1.3e+10
S_{top} 1.3e+09
S_{top} 1.3e+10
Normalized PL Intensity [a.u.]
Time after Pulse [ns]
Parameter Histograms
(b) k_{rad} [cm^{3}s^{-1}]
3.9 (3.6 — 21.5) ×10^{-10}
(c) $k_{eff, bulk}$ [s^{-1}]
nr: 5.9 (3.3 — 21.4) ×10^3
nr+rad: 8.2 (7.8 — 30.1) ×10^5
(d) SRV [cm s^{-1}]
S_{bot}: 5.1 (0.1 — 5.5) ×10^1
S_{top}: 8.6 (1.8 — 9.2) ×10^1
Sample Frequency [a.u.]
(e) μ_{vert} [cm^2 (Vs)$^{-1}$]
cannot be inferred
(f) k_{nr} [s^{-1}]
k_d: 5.9 (3.3 — 21.4) ×10^3
(g) $p_{eq, min}$ [cm^{-3}]
7.7 (0.6 — 8.7) ×10^{14}
(i) L_D [μm]
cannot be inferred
(j) -log(LL)$_{av.}$ [-]
4.7 (4.5 — 4.9) ×10^{-1}
(k) $f_{\sigma LL}$ [-]
2.0 (2.0 — 2.0) ×10^0

Supplementary Figure 24. Carrier dynamics of the MACl + $PbCl_2$ sample. **a**, TRPL decays measured from both the top (perovskite-air interface) and substrate (glass/ITO/HTL) sides. **b–k**, The normalised probability distributions for all parameters extract from the Bayes-MCMC, including the radiative recombination rate (k_{rad}), effective non-radiative bulk recombination rate ($k_{\text{eff, nr, bulk}}$), surface recombination rate (SRV), vertical mobility (μ_{vert}), non-radiative recombination rate via a deep bulk defect (k_{d}), equilibrium hole density under pulsed excitation (p_{eq}), diffusion length (L_{D}), average log-likelihood for the dataset ($-\log(LL)_{\text{av}}$), and $f_{\sigma\text{LL}}$.

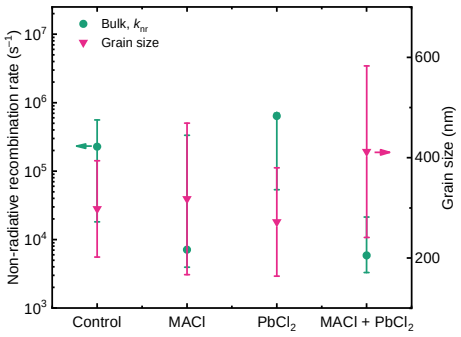

Supplementary Figure 25. Carrier dynamics. The inferred non-radiative bulk recombination rate (displayed also in **Fig. 3b**) and grain sizes for the control, MACl, $PbCl_2$, and MACl + $PbCl_2$ perovskite deposited on glass/ITO/HTL substrates.

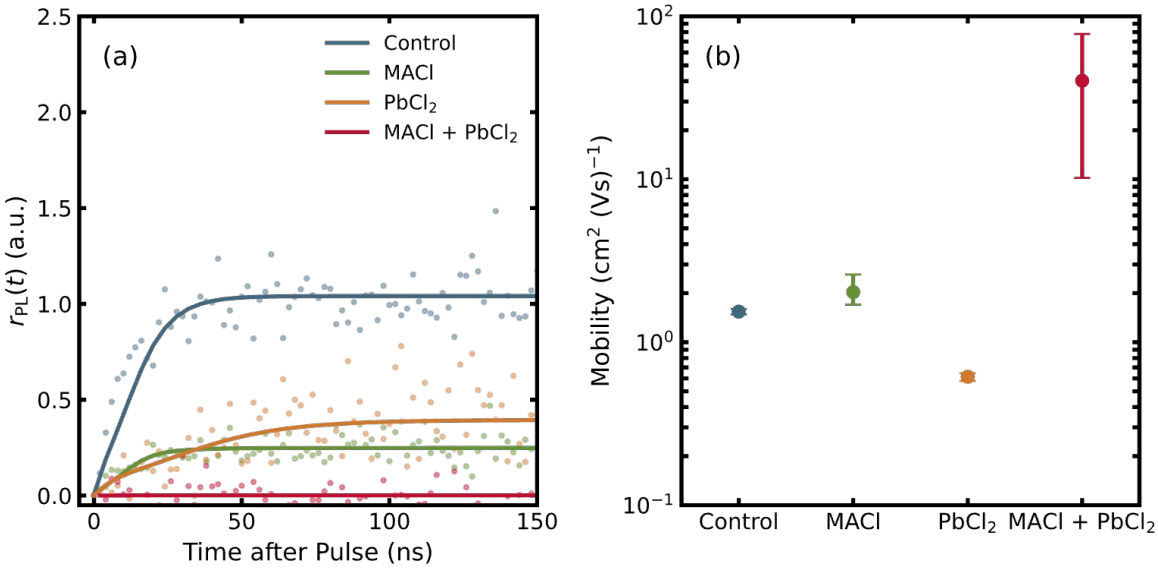

Supplementary Figure 26. Vertical charge-carrier mobility. **a**, The ratio of the TRPL decay as a function of time, measured from the red (850 nm) and blue (750 nm) emissions individually. The laser fluence used was 1.3×10^{10} cm^{-2}. To estimate the spectral shift of the PL, measurements were taken from the perovskite side. The fitting curves of the diffusion model (**Methods**) are shown as solid lines. **b**, The inferred vertical mobility of control, MACl, $PbCl_2$, and MACl + $PbCl_2$ samples. The points are the median data and the error bars indicate the first and third quartiles.

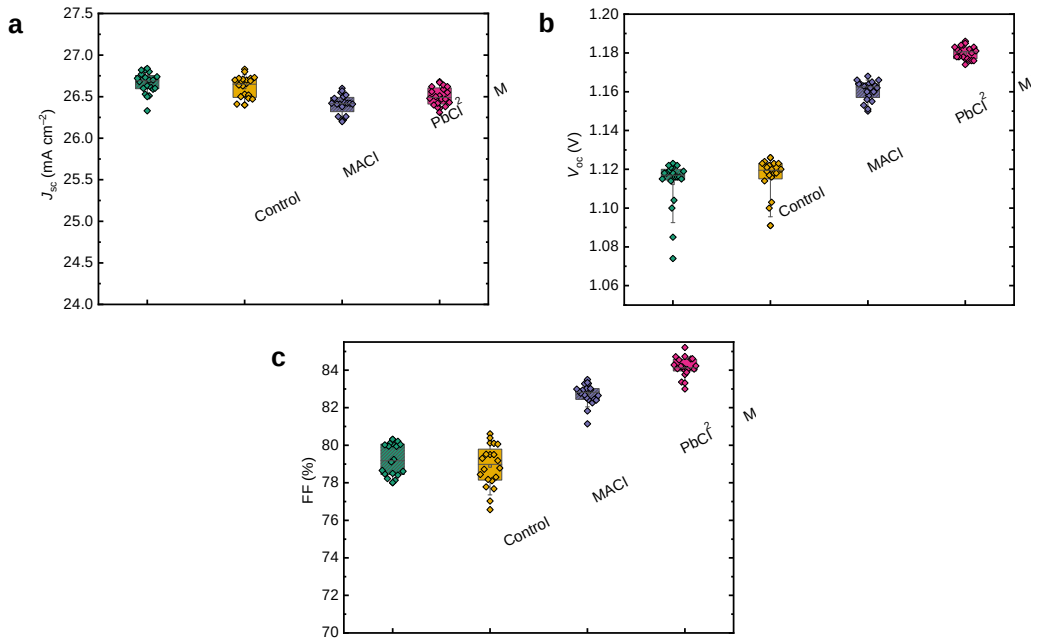

Supplementary Figure 27. Photovoltaic performance (reverse scans) of control, MACl, $PbCl_2$, and MACl + $PbCl_2$ PSCs (0.05 cm^2). For each variation at least 20 devices were shown. In the boxplots, the mean (open square), median (center line), 25th and 75th percentiles (box limits), minimum (–) and maximum (+), outliers (△), and 10th and 90th percentiles (whiskers) are shown.

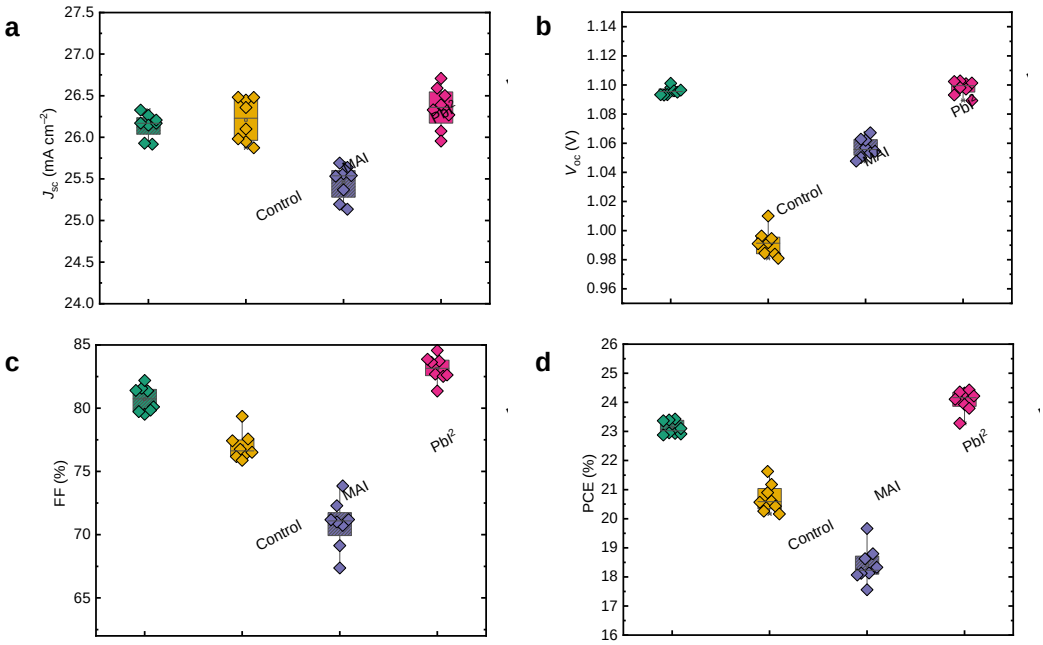

Supplementary Figure 28. Photovoltaic performance (reverse scans) of control, MAI, PbI_2, and MAI + PbI_2 PSCs (0.05 cm^2). For each variation 8 devices were shown. In the boxplots, the mean (open square), median (center line), 25th and 75th percentiles (box limits), minimum (–) and maximum (+), outliers (△), and 10th and 90th percentiles (whiskers) are shown.

福建省计量科学研究院
FUJIAN METROLOGY INSTITUTE
（国家光伏产业计量测试中心）
National PV Industry Measurement and Testing Center

报告编号： 25Q3-00228
Report No.

检测结果/说明：
Results of Test and additional explanation.

3.Measurement Data and Curves for MPPT under STC

η (%)	26.41
P_{MPP} (mW)	1.294
I_{MPP} (mA)	1.234
V_{MPP} (V)	1.049

Note: Measurement data for MPPT under STC in the above table was the mean value acquired during the final 30 seconds of the 300 seconds test

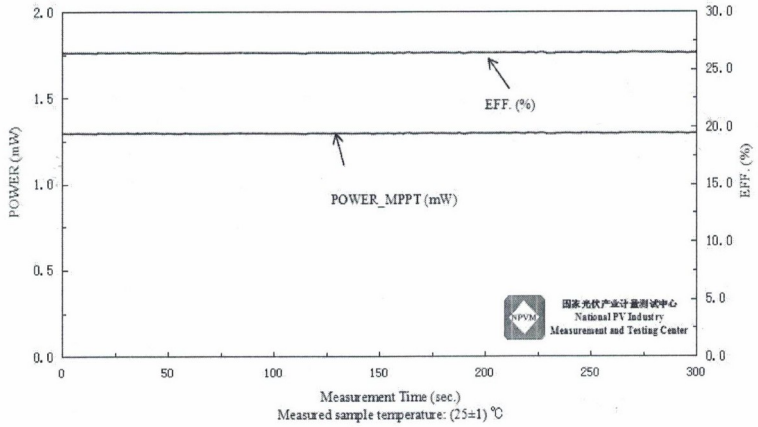

Figure 2. Measurement curves of the measured sample for MPPT

Supplementary Figure 29. Certified results for 0.05 cm² p-i-n device. The device delivers a mean MPPT efficiency of 26.4% during 300 s.

福建省计量科学研究院
FUJIAN METROLOGY INSTITUTE
（国家光伏产业计量测试中心）
National PV Industry Measurement and Testing Center

报告编号：23Q3-00316
Report No.

检测结果/说明：
Results of Test and Additional Explanation.

3 Measurement Data and Curves for MPPT under STC

η (%)	24.51
P_{MPP} (mW)	25.42
I_{MPP} (mA)	25.24
V_{MPP} (V)	1.007

Note: Measurement data for MPPT under STC in the above table was the mean value acquired during 300 seconds.

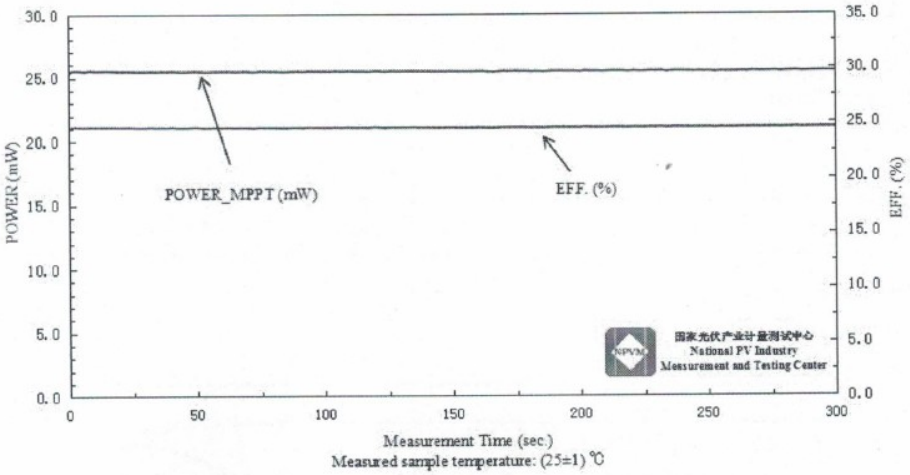

Figure 2. Measurement curves of the measured sample for MPPT

Supplementary Figure 30. Certified results for 1 cm² p-i-n device. The device delivers a mean MPPT efficiency of 24.51% during 300 s.

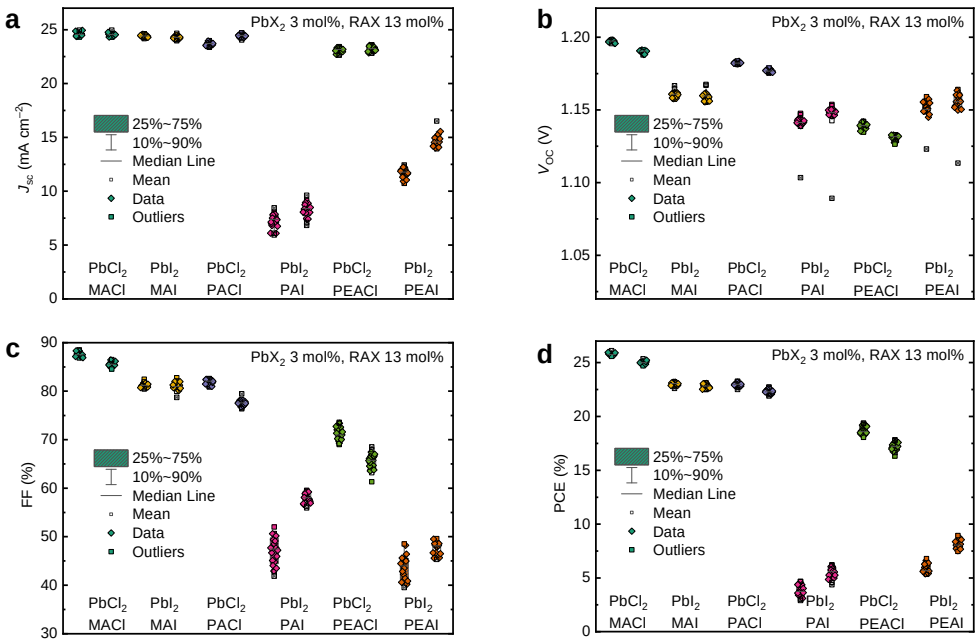

Supplementary Figure 31. Photovoltaic performance of 3 mol% PbX_2 + 13 mol% RAX (X = I or Cl, RA = methylammonium, propylammonium, or phenethylammonium) added PSCs (0.05 cm^2). For each variation at least 15 devices are shown. In the boxplots, the mean (open square), median (centre line), 25th and 75th percentiles (box limits), minimum (–) and maximum (+), outliers (△), and 10th and 90th percentiles (whiskers) are shown. For each condition, the left column displays results under reverse scans, and the right column shows results under forward scans.

Supplementary Table 1. Position and FWHM values of the (100) peak acquired from the 1D XRD patterns.

	Position (°)	FWHM (°)
Control	13.94	0.209
MACl	13.96	0.205
$PbCl_2$	13.98	0.212
MACl + $PbCl_2$	13.956	0.207

Supplementary Table 2. Atomic concentration (%) derived from XPS measurements.

Sample	C	N	O	Cl	I	Pb
Control	38.59	14.41	6.94	0.00	31.70	8.36
MACl	40.32	15.52	7.49	1.14	28.15	7.38
$PbCl_2$	43.26	10.87	7.28	1.59	29.35	8.65
MACl + $PbCl_2$	48.02	11.98	8.14	1.73	23.54	6.59

Supplementary Table 3. Normalised intensity of Cl^- ($I_{Cl,norm.}$) relative to I^- determined from ToF-SIMS measurements**.**

	Normalised intensity ($I_{Cl,norm.}$)			
Depth	Control	MACl	$PbCl_2$	MACl + $PbCl_2$
0 nm	1.71×10^{-3}	1.25×10^{-2}	2.44×10^{-1}	1.70×10^{-1}
10 nm	1.69×10^{-5}	2.22×10^{-2}	8.63×10^{-2}	1.38×10^{-1}
Average	8.64×10^{-4}	1.73×10^{-2}	1.65×10^{-1}	1.54×10^{-1}

Supplementary Table 4. Relative sensitivity factor of Cl estimated for each sample.

Sample	C_{Cl} (%)	$I_{Cl,norm.}$	γ_{Cl}	RSF_{Cl}
Control	0	8.64×10^{-4}	0.758	0
MACl	1.14	1.73×10^{-2}	0.758	49.9
$PbCl_2$	1.59	1.65×10^{-1}	0.758	7.30
MACl + $PbCl_2$	1.73	1.54×10^{-1}	0.758	8.51

Supplementary Table 5. Pseudo-*JV* parameters perovskites obtained from half-cells.

Tandem cells	Ideality factor, n	V_{OC} (V)	FF	PCE (%)
Control Half cell	1.09	1.201	0.887	28.1
MACl + $PbCl_2$ Half cell	1.05	1.226	0.889	28.8
Control Full cell	1.21	1.143	0.868	26.2
MACl + $PbCl_2$ Full cell	1.09	1.191	0.881	27.7

References

1. Chen, H., et al. Quantum-size-tuned heterostructures enable efficient and stable inverted perovskite solar cells. *Nat. Photonics* **16**, 352–358 (2022).
2. Hu, S., et al. Optimized carrier extraction at interfaces for 23.6% efficient tin–lead perovskite solar cells. *Energy Environ. Sci.* **15**, 2096–2107 (2022).
3. Hu, S., et al. A Universal Surface Treatment for p–i–n Perovskite Solar Cells. *ACS Appl. Mater. Interfaces* **14**, 56290–56297 (2022).
4. Chen, H., et al. Regulating surface potential maximizes voltage in all-perovskite tandems. *Nature* **613**, 676–681 (2023).
5. Wang, Z., et al. Suppressed phase segregation for triple-junction perovskite solar cells. *Nature* **618**, 74–79 (2023).
6. Hu, S., et al. Steering perovskite precursor solutions for multijunction photovoltaics. *Nature* **639**, 93–101 (2024).
7. Chen, H., et al. Improved charge extraction in inverted perovskite solar cells with dual-site-binding ligands. *Science* **384**, 189–193 (2024).
8. Maj, P., Grybos P., Szczygiel R., Taguchi T., Nakaye Y., Kobayashi S. HyPix-3000 - a large area single-photon counting detector with two discriminator thresholds. In: *2014 IEEE Nuclear Science Symposium and Medical Imaging Conference (NSS/MIC)* (2014).
9. De La Peña, F., et al. hyperspy/hyperspy v1.4.1. *Zenodo*, 10.5281/zenodo.1469364 (2018).
10. Dasgupta, A., et al. Visualizing Macroscopic Inhomogeneities in Perovskite Solar Cells. *ACS Energy Lett.* **7**, 2311–2322 (2022).
11. Maiberg, M., Scheer R. Theoretical study of time-resolved luminescence in semiconductors. II. Pulsed excitation. *J. Appl. Phys.* **116**, 123711 (2014).
12. Fai, C., Ladd A. J. C., Hages C. J. Machine learning for enhanced semiconductor characterization from time-resolved photoluminescence. *Joule* **6**, 2585–2610 (2022).
13. Cho, C., et al. Efficient vertical charge transport in polycrystalline halide perovskites revealed by four-dimensional tracking of charge carriers. *Nat. Mater.* **21**, 1388–1395 (2022).
14. Kober-Czerny, M., et al. Determining Parameters of Metal-Halide Perovskites Using Photoluminescence with Bayesian Inference. *PRX Energy* **4**, 013001 (2025).